Power Density Distributions in Electron Beams

The EMFC electron beam measurement method FWe2 is compared to the ISO standard for a second-moment D4σ calculation of the beam diameter

BY J. W. ELMER, A. T. TERUYA, AND G. GIBBS

Abstract

Measuring and controlling the power density distribution of electron beams used for welding is critical for producing repeatable welds and for transferring welding parameters between different machines. On any given machine, the power density distribution is controlled by defocusing the beam relative to its sharpest focused condition. However, measuring the power density distribution can be difficult due to the intense nature of welding beams and is further complicated by imperfect electron optics that can distort the beam, making it difficult to quantify. The enhanced modified Faraday cup (EMFC) diagnostic method was used here for beam analysis that utilizes computed tomography to reconstruct the beam's power density distribution. These results were compared to the International Standards Organization (ISO) method for characterizing laser beams using a second-moment D4σ calculation. For ideal Gaussian-shaped beams, both methods would give the same result. However, for imperfect beams, the calculated D4σ diameter was shown to be about 25% larger relative to the FWe2 diameter measured by the EMFC due to the heavier weighting of data in the tails of the beam by D4σ. Although both methods produce repeatable welds, it is important to understand the differences in the reported beam diameters, divergence angles, and beam parameter products when transferring parameters between machines.

Keywords

- Electron Beam Diagnostics
- FWe2
- FWHM
- D4σ
- Second-Moment Calculations
- Divergence Angle
- Beam Caustic
- Beam Parameter Product (BPP)
- Rayleigh Length
- Gaussian Beams
- Beam Astigmatism

Introduction

Most modern electron beams used for welding are generated in a high-voltage triode assembly that contains a negatively charged cathode that generates the electrons, a beam-focusing bias cup of the same electrical charge, and an anode of positive electrical charge that accelerates the electrons to high voltages, typically between 50 and 150 kV (Refs. 1, 2). The electron beam is generated by resistively heating the cathode to the point where thermionic emission takes place to create a cloud of electrons that can be emitted from the cathode and accelerated toward the anode to form the beam. The beam current is regulated through the charge applied to the bias cup, allowing electrons to be emitted from the cathode. After the beam passes through the anode, it is focused and deflected using a series of electromagnetic coils to bring the beam to a sharp spot on the surface of the part being welded. Cathodes for electron beam welding machines are made of high melting point materials, such as tungsten, tungsten-rhenium, or tantalum, and have different geometric shapes depending on the electron gun, maximum beam current, and desired lifetime. The cathode shape influences the final beam shape and typical geometries, including ribbon filaments with a square or rectangular face, circular foil cathodes, or rod cathodes with a circular shape. Some designs may include holes in the center of the cathode face to prevent a central hot spot or thin wire filaments (hairpin), which are largely outdated due to a limited lifetime (Ref. 3).

Figure 1A shows a photograph of a ribbon filament cathode positioned in the electron beam gun of the Hamilton Standard electron beam (EB) welding machine (HS#605) at Lawrence Livermore National Laboratory (LLNL), Livermore, Calif. The ribbon filament strip was fabricated into a V-configuration
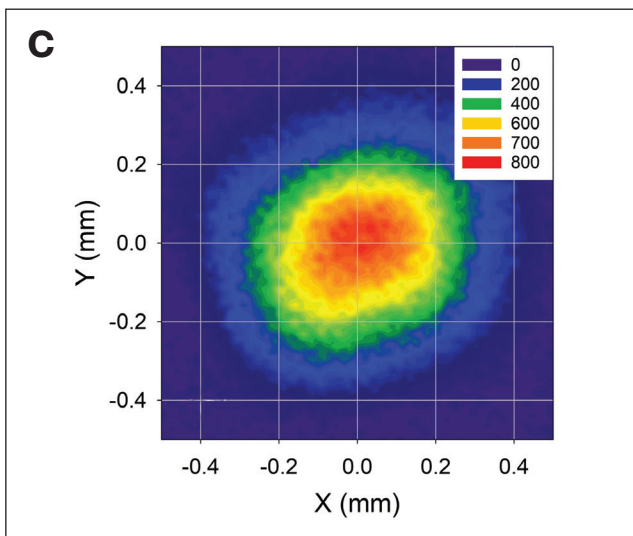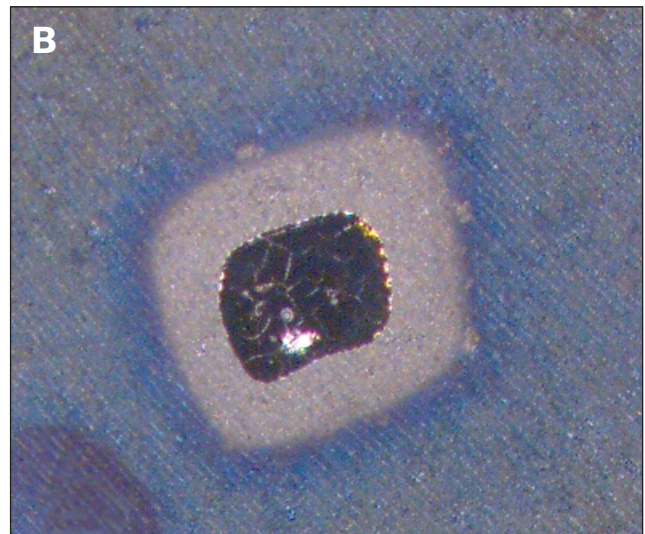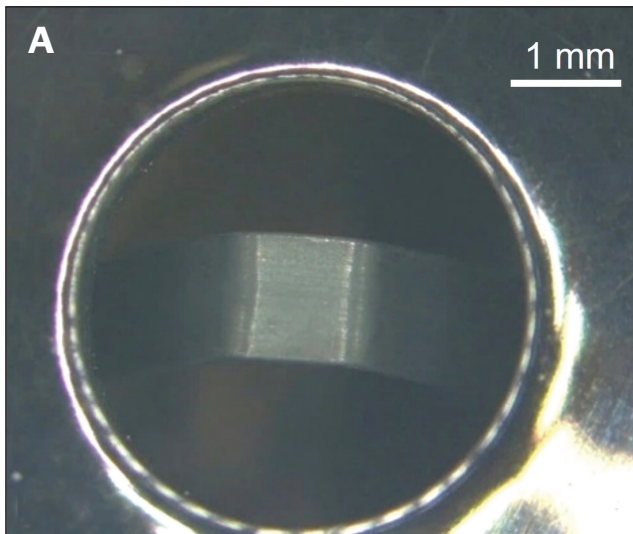
A 1 mm

B

C

Fig. 1 — A — Photograph of a ribbon filament inserted into the circular aperture of the electron beam gun; B — photograph of a burn pattern of this filament onto a tungsten-focusing block; C — EMFC electron beam power density distribution of the beam (scale in W/mm²).

with a flat bottom, resulting in a rectangular-shaped emitting surface that is centered in the aperture of the electron gun with the filament legs attached to the electrical circuit for resistive heating. During operation, electrons emitted from the rectangular shape were focused back onto the surface being welded, roughly maintaining the geometric shape of the emitting surface as the beam propagated down the column. Figure 1B shows this result, where a burn pattern is made from the well-aligned filament shown in Fig. 1A onto a tungsten block. This burn pattern was made with a short-duration, 1.5-kW (15-mA, 100-kV) beam that was defocused +40 mA (706 mA) to prevent the beam from drilling into the tungsten. The rectangular shape of the filament's emitting surface (~1 × 1.3 mm [~0.039 × 0.051 in.]) is reproduced onto the tungsten target, confirming that the filament is well

positioned in the gun and that the beam is well aligned in the column. But the power density distribution of the beam could not be determined from an image like this alone. Diagnostics were used for this purpose, and Fig. 1C shows the measured current density distribution of this beam, using the enhanced modified Faraday cup (EMFC) diagnostic, to be described in more detail later. The EMFC quantifies the beam's power distribution using radial slits and computed tomography (Ref. 4) as opposed to pinhole apertures that are commonly used in other devices when the beam can be scanned over the pinhole at very high rates (Ref. 5).

Increasing or decreasing the size of the electron beam spot is performed by increasing or decreasing the electrical current passing through the final electromagnetic focusing lens. This effect moves the sharp focal point up or down in the chamber (as illustrated in Fig. 2), which has a large effect on keyholing and the penetration depth of the weld (Refs. 6, 7). The main effect of focus is that by reducing the current in the final focusing lens (underfocusing or negative defocus) relative to the sharp-focus crossover current, the beam is not as intensely focused by the magnetic field. This drops the sharp focal spot lower in the chamber, creating a converging beam on the surface being welded. The opposite is true for higher-focusing coil currents relative to the sharp-focus condition (overfocusing or positive defocus), which raises the sharp focal spot in the chamber and creates a diverging beam relative to the surface being welded. The hourglass shape of the beam that focuses to a sharp spot at the full angle, Θ, is known as the beam's caustic, which defines the envelope of the propagating beam and is an important factor in understanding how the beam shape changes with defocus settings and the depth of field of the beam (Refs. 8, 9).

In an ideal electron optical configuration, the electron beam gun's focusing lenses and deflection coils would be perfectly aligned and provide uniform magnetic fields, keeping the cross-sectional shape of the beam constant as it propagates in the welding chamber. Such a perfect system would image the electron beam emanating from the cathode onto the surface of the part being welded, maintaining its original geometric shape and charge distribution, as shown in Fig. 1, but expanded or contracted in size by distance from the final

focusing lens, as illustrated in Fig. 2. Unfortunately, perfect electron optical systems and perfect and constant cathode electron emissions do not exist, which results in astigmatism or other imperfections into the beam. These and other factors create uncertainty in the final charge distribution in the focused spot used for welding, particularly for filaments that are not properly inserted into the gun, beams that are misaligned in the column, and filaments that are developing hot spots due to wear and age or do not have sufficient filament current, etc. (Refs. 1, 9, 10). Because of this, having reliable diagnostics to measure the final electron charge distribution is critical to creating repeatable welds on the same machine through filament changes and time and for transferring weld parameters from one machine to another (Refs. 4, 5, 11–13).

Electron Beam Diagnostics and Beam Measurements

Enhanced Modified Faraday Cup

The EMFC measures the current density distribution in electron beams by deflecting the beam over a radially oriented slit-disk diagnostic in a circular pattern to create profiles of the beam that can be reconstructed using a computed tomographic (CT) method (Refs. 3, 4, 14, 15). The standard EMFC uses a 17-slit disk to create 17 profiles of the beam,
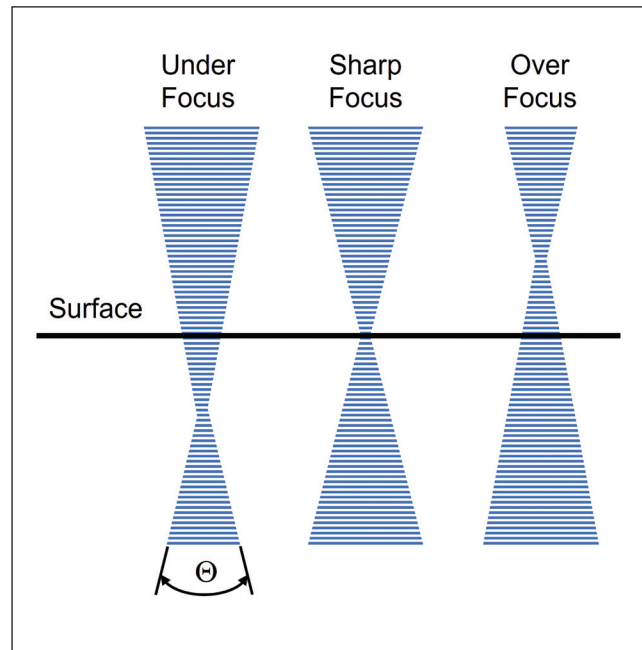
Fig. 2 — Representation of underfocused and overfocused beams on the position of the sharp focus crossover spot, relative to the surface where the beam is being measured or where the part is being welded.

Table 1 — Summary of Different Methods Used to Describe Gaussian Shapes Related to the Standard Deviation of an Ideal Circular Gaussian Distribution

Parameter	Fraction of Peak Power, P_o, at the Measured Width	Relationship to σ	Percentage of the Gaussian Area
2σ	0.605	2.0σ	39.6
FWHM	$0.500 = (P_o/2)$	$2\sqrt{2\ln(2)} * \sigma = 2.35\sigma$	50.0
3σ	0.324	3.0σ	67.7
D4σ	0.135	4.0σ	86.5
FWe2 = D4σ = D_{86}	$0.135 = (P_o/e^2)$	4.0σ	86.5
FWTM	$0.100 = (P_o/10)$	$2\sqrt{2\ln(10)} * \sigma = 4.29\sigma$	90.1

Note: Highlighted cells correspond to the definition of a given parameter.
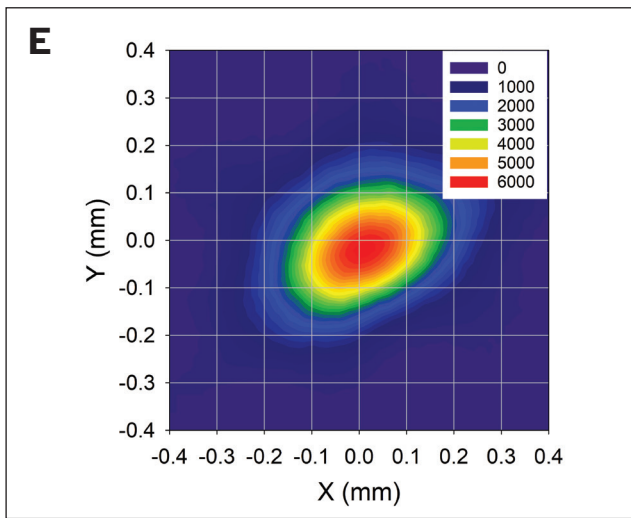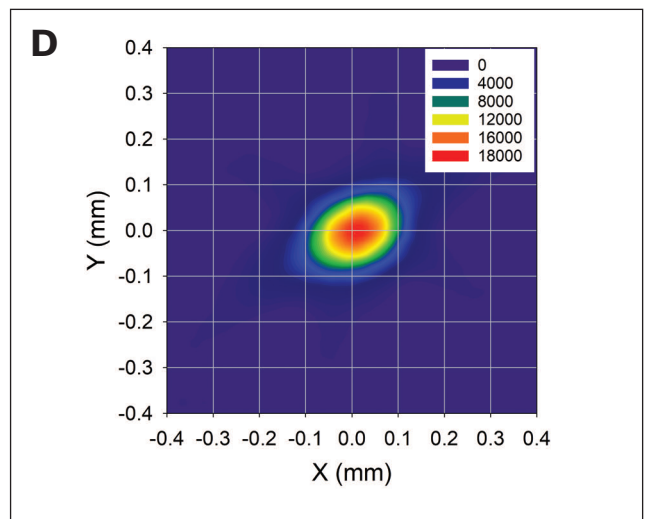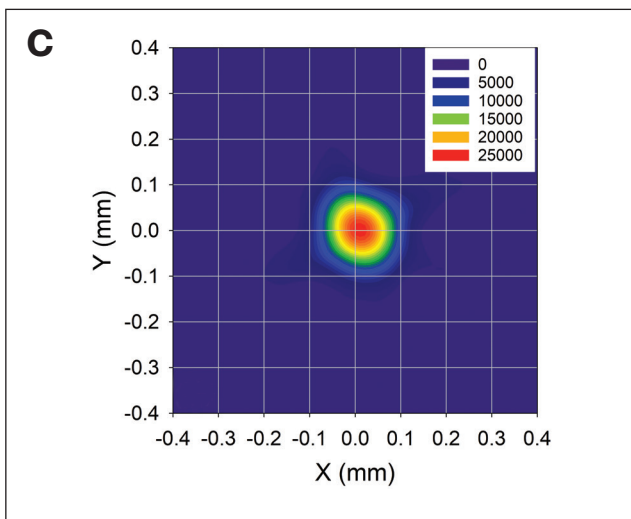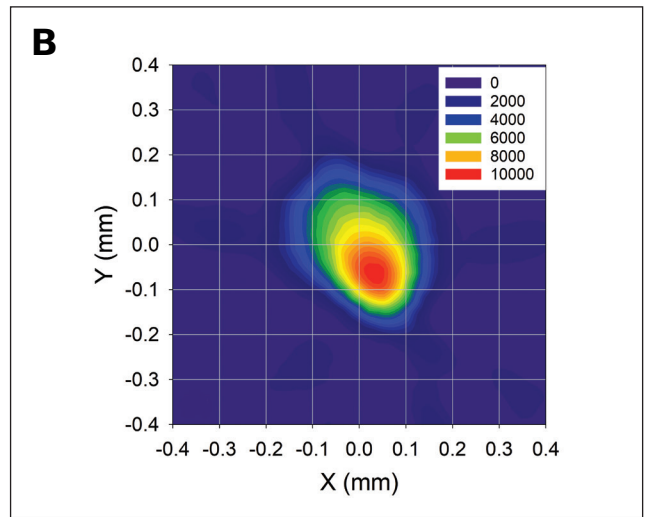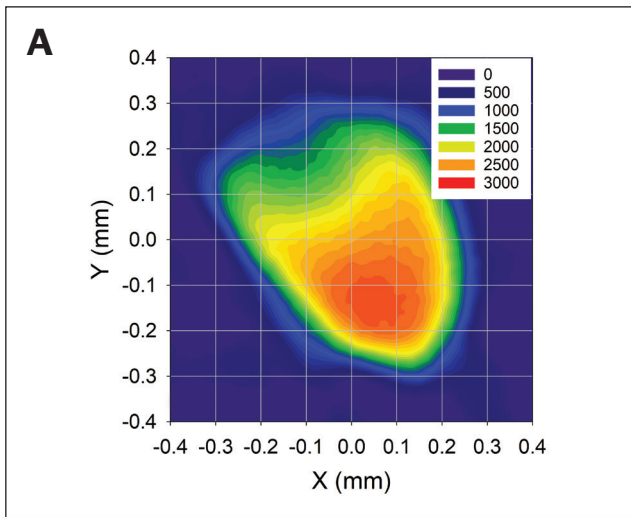
Fig. 3 — EMFC contour plots of the 120-kV, 5-mA, misaligned beam showing the beam converging to, and diverging from, sharp focus: A — −20; B — −10; C — sharp; D — +10; E — +20 mA focus settings. Data legends are in W/mm², and note the change in the color scales between images.

viewed from different angles that are acquired by a fast-acting data acquisition system and laptop computer. The number of slits is optimized at 17 for typical EB machines with beam diameters that vary from about 0.25 mm (0.01 in.) in the sharp-focused condition to produce deep welds to about 2 mm (0.079 in.) defocused beams used to produce cosmetic or shallow welds. Higher CT resolution is possible with higher numbers of slits, but the maximum beam diameter that can be examined becomes smaller to ensure that the beam is passing through only one slit at a time (Refs. 4, 15).

To minimize heat damage to the slit disk and EMFC diagnostic assembly, profiles were collected by rapidly rotating the beam in a circle (typically 85 Hz) over the diagnostic, and the data acquisition system captured data on the order of 500,000 samples/s to provide the high-resolution data. A first-moment calculation, which will be discussed in more detail later, was then performed on each profile so that the centroid of each peak laid in the center of the reconstruction window. The individual profiles were normalized to all have the same area (equal to the integrated beam current) as the beam passed over a given slit, which allowed for slight variations in the effective slit widths or nonperpendicularity of the beam with respect to the slit. Next, the profiles were

Table 2 — Summary of EMFC Data Taken on the 600-W (120-kV, 5-mA) Beams Shown in Fig. 3

Parameter	Units	Relative Focus (mA)				
		+20	+10	0	−10	−20
Lens Current	mA	796	786	776	766	756
EMFC Data						
FWe2 min.	mm	0.39	0.22	0.23	0.33	0.57
FWe2 maj.	mm	0.62	0.38	0.25	0.43	0.75
Ellipticity	—	0.61	0.57	0.96	0.76	0.76
Major Angle	deg	35	26	37	−59	−52
PPD	W/mm^2	6090	17,700	24,900	9990	2800
FWHM*	mm	0.27	0.16	0.14	0.22	0.49
FWe2*	mm	0.49	0.28	0.24	0.37	0.64
Gaussian Fit						
PPD	W/mm^2	6032	17,856	25,027	9791	3036
FWHM (2.35σ)	mm	0.295	0.169	0.133	0.191	0.317
FWe2 (4σ)	mm	0.502	0.288	0.226	0.325	0.540
R^2	—	0.999	0.999	0.999	0.996	0.982
PPD$_{meas}$/PPD$_{Fit}$	%	101	99.0	99.5	102	92.2

Note: The data were taken at the crossover focal length of 242 mm with lens current of 776 mA.

A

B

C

D

E
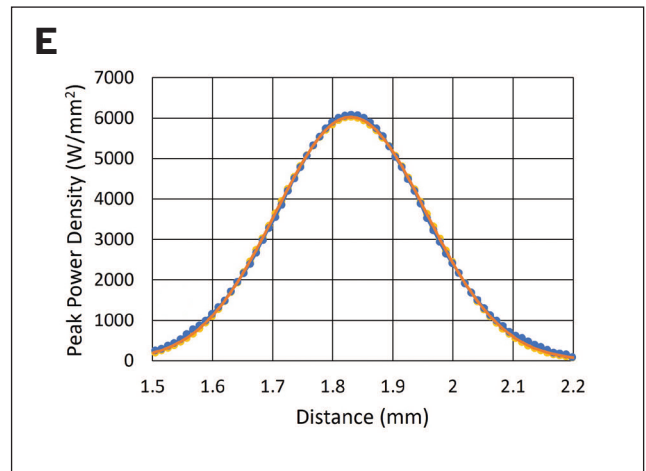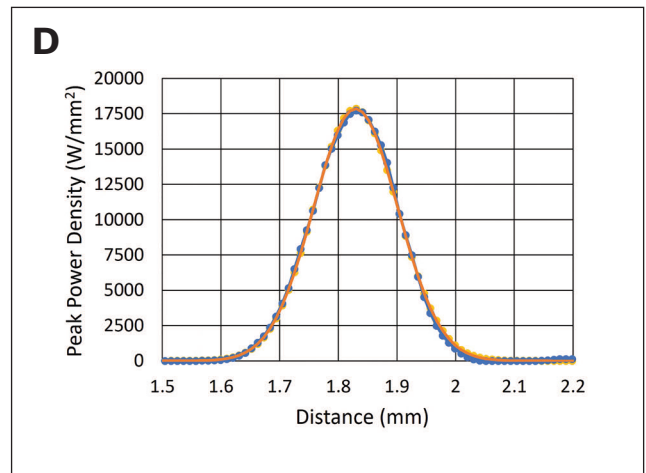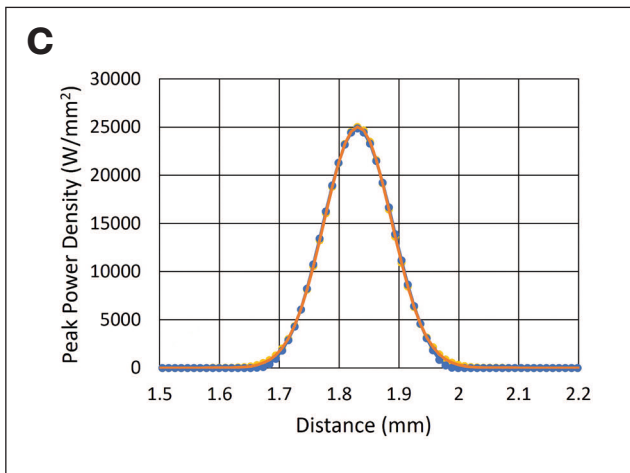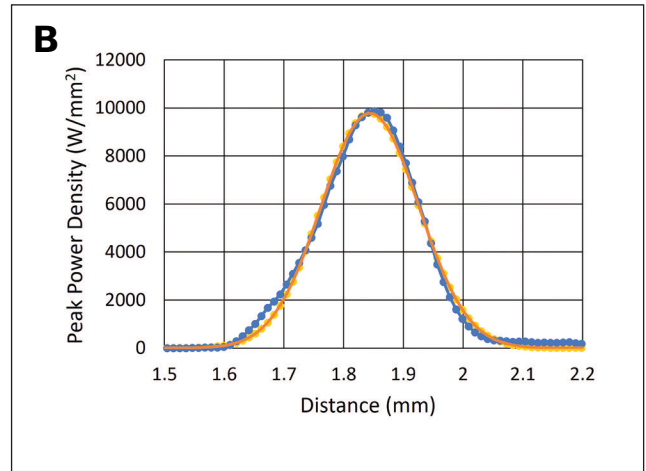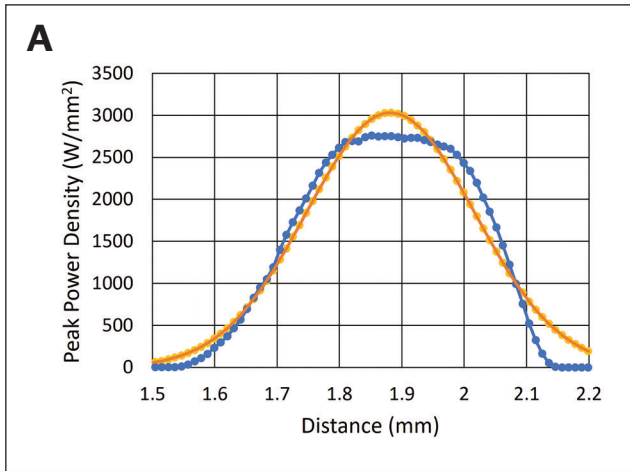
CT-reconstructed using a filtered back-projection method, as detailed by Teruya et al. (Ref. 14), to create a 3D representation of the current density distribution (mA/mm²) over the x-y plane. Finally, the 3D distribution was normalized to its integral, equaling the total beam current. Once completed, statistical analysis of the beam could be performed to measure the beam's diameter and other features. The total power of the beam (kW) was equivalent to the beam current multiplied by the accelerating voltage, which typically has values between 50–150 kV, depending on the type of machine and desired weld properties.

The electron beam current density distributions of welding beams tend to be Gaussian-shaped with some astigmatism that makes them noncircular. The most common noncircular shape tends to be elliptical with an aspect ratio (minor/major diameter ratio) of less than 0.87. Values between 0.87 and 1.0 are considered to be circular (Ref. 8). The elliptical astigmatic shape rotates its orientation 90 deg as it passes through the sharp focal position (Refs. 3, 16) and can be mathematically defined by a relatively simple analytic expression of the current density distribution across the major and minor axes of the ellipse, as described in Equation 1. Note that this relationship was developed for laser beam propagation (Ref. 17), where its electric field distribution (E_o) has been replaced with the electron beam's current density distribution.

Fig. 4 — Profiles through the peak of each of the power density distribution plots shown in Fig. 3. The blue line with markers is the measured EMFC profile, while the orange line is the Gaussian least squares regression fit through the data: A — −20; B — −10; C — sharp; D — +10; E — +20 mA focus settings. Note the changes in the power density axis scales.

$$J(x, y) = I_0 \exp[((-(x - a)^2)/2\sigma_x^2) + ((-(y - b)^2)/2\sigma_y^2)] \quad (1)$$

In this expression, $J(x,y)$ is the current density of the beam, x and y are the spatial coordinates, σ_x and σ_y are the standard deviations of the Gaussian distribution along the major and minor axes, I_o is the peak of the Gaussian, while a and b are positions of the center of the Gaussian peak. The astigmatism tended to become less pronounced as the beam was imaged closer to its sharpest focus condition, where the beam crossed over from a converging to a diverging beam. In this region, the different astigmatic focal points that created the elliptical shape laid above and below sharp focus, and the effects averaged out between these two points (Ref. 3). Other arbitrary beam shapes that were not able to be characterized by analytic expressions were handled by second-moment calculations, as detailed in the next section.

The EMFC software takes the reconstructed beam data and initially analyzes it to determine the full width of the beam at one-half its maximum power density (FWHM) and also a second parameter, FWe2, which is considered to be the beam diameter and is the full width of the beam at $1/e^2$ of its maximum power density. For an ideal Gaussian beam, Table 1 indicates that the FWHM is 2.35 times higher than the standard deviation of the Gaussian distribution, σ, while FWe2 is the effective beam diameter with a value of 4.0 σ. The fraction of the beam's power bounded by a given beam diameter can be calculated by integrating Equation 1 over the definite limits of a given beam cross section, and such a calculation shows that the FWHM contains 0.500 fraction of the beam's power, while FWe2 contains 0.865 fraction of the beam's power ($1-1/e^2$). For noncircular beams, an angle along the major axis of the distribution is determined relative to the electron beam chamber, and an ellipticity value is calculated by the EMFC as the ratio of the major to minor axes of the distribution. In addition, a calculation of the peak power density (PPD) of a perfect Gaussian beam can be made and compared to the measured beam as an indication of how Gaussian-like the beam is. A more precise determination of the Gaussian shape can be found by regression analysis for the R^2 coefficient of determination value of the Gaussian fit.

Additional measures of Gaussian beam widths can be made relative to the standard deviation of the Gaussian. These representations are summarized in Table 1 for comparison. D4σ is a commonly used method for estimating the beam diameter, as detailed in ISO 11146-1:2021, *Lasers and laser-related equipment — Test methods for laser beam widths, divergence angles and beam propagation ratios — Part 1: Stigmatic and simple astigmatic beams*, where it is calculated using a second-moment method for noncircular astigmatic beams (Ref. 8). FWe2 and D_{86} are also used to represent the beam diameter and are equivalent to D4σ for an ideal circular Gaussian beam containing 86.5% of the beam's power. Note that there appears to be some confusion in the literature over these definitions, but to the authors' knowledge, the relationships presented in Table 1 are mathematically accurate per the intent of the original definition. Furthermore, note that the percentage area under a Gaussian beam is different and less than what would be calculated for a standard normal Gaussian distribution used in conventional probability and statistics due to the fact that the Gaussian integration for the beam is performed over two spatial coordinates (x and y or R and Θ), whereas standard probability calculations are performed over a single coordinate (typically defined as z), where the fraction under the curve works out differently with respect to the standard deviation.

While all these statistics are useful in understanding the beam and its properties, in practicality, a simpler method is often desired for estimating its intensity. Such a method was particularly useful for production applications in which decisions or comparisons needed to be made quickly about the repeatability of the beam over time on the same machine to generate welds of the desired quality. For this purpose, a FWHM* and FWe2* were calculated from the EMFC-reconstructed beam data. FWHM* is the FWHM of a circular Gaussian beam that has the same area as that of the measured elliptical shape and has a value that falls between the minimum and maximum extremes. Likewise, FWe2* is defined as the FWe2 of a circular Gaussian beam that has the same area of the measured elliptical shape at $1/e^2$ of the PPD and is used here to represent the effective beam diameter for comparison with other data or for transfer of parameters from one machine to another. For an ideal circular Gaussian beam, FWe2* would equal the D4σ.

One example of data measured by the EMFC for a noncircular beam is shown in the contour plots of Fig. 3, where a 600-W (120-kV, 5-mA) beam was analyzed between plus and minus 20 mA of the sharp-focus position. This data represents a typical series of defocused beam shapes for a slightly misaligned beam using a W-Re ribbon filament (CL-167-R with a ~1 × 1.3-mm emitting surface) in the electron beam welding machine HS#605 fitted with a R-40 gun as detailed (Refs. 4, 18). The initial sharp focus crossover was located at 776 mA by the operator and verified by the EMFC using the 17-slit disk with 0.004-in. (0.1-mm)-wide slits. The ± 20 mA of defocus represents approximately a doubling of the sharp-focused beam diameter with a corresponding 4× increase in the beam area at a focal length of 242 mm (9.53 in.) on this machine. This range of defocus contains the crossover region and exceeds the Rayleigh length of the beam in which the area would be expected to increase by only 2× for an ideal Gaussian shape with a √(2) increase in beam diameter (Refs. 8, 9). Visually, the effect of defocus on the beam size was clear as it came into sharp-focus with a minimum diameter, FWe2*, of 0.24 mm (0.009 in.). The beam was not symmetric above the sharp focus, where it flared out and increased in size more rapidly at the minus defocus settings, likely due to a misalignment of the beam and the optical components in the upper column of the gun. The data shown in Fig. 3 are quantified in Table 2, showing the measured beam statistics, which indicated a rotation of the major axis of the ellipse of approximately 90 deg as it crossed over the sharp-focal position, and that the beam became more circular, smaller, and intense near the sharp-focus position.

The Gaussian-like nature of the beam can be estimated by taking EMFC line profiles across the peak and fitting them to a Gaussian relationship to optimize σ, b, and I_o and compare the fitted value to the measured data. Equation 2 shows this

relationship for a line profile parallel to the Y-axis and through the peak of the beam in the following:

$$J(x_0, y) = I_0 \exp[((-(y - b)^2)/2\sigma_y^2)] \qquad (2)$$

In this equation, σ_y represents the standard deviation of the fit for profiles vertically up and through the center of the beams, I_o represents the PPD of the fit, and b represents the center of the Gaussian fit peak. These calculations were performed on each of the beams shown in Fig. 3, and the results are shown in Fig. 4, where the blue lines with markers are the EMFC data points and the solid orange line is the ideal Gaussian fit to the data. The Gaussian-like nature of the beam was clear, being only significantly different from a true Gaussian at the –20-mA defocus position, where the underfocused beam was measured above and was furthest away from the sharp focus. The coefficient of determination, R^2, values for these fits are shown in Table 2, indicating very high correlations for all the beams except at the –20 mA focus position, where the R^2 dropped off to 0.982. In addition, a Gaussian-like quantity can be calculated as the ratio of the measured PPD of the beam to the ideal PPD based on the value of the ideal fit. The last line of Table 2 summarizes these data, where the difference is 100 ± 1% for positive-defocused and sharp-focused beams but drops off to 92.2% for the –20 mA-defocused beam. These data further confirmed that the beam was substantially Gaussian-like for positive defocus settings used in this study but became less Gaussian-like for increasing underfocused settings for this beam.

As a final figure in this set of comparisons, the CT recon-structed beam data can be postprocessed to quantify and plot the power density distribution in a 3D format. Figure 5 shows one of the plots for the sharp-focused, 600 W beam with a PPD of 24,900 W/mm². The corresponding contour plot with pseudocolor intensities is shown above the 3D plot and illustrates the Gaussian-like nature of these beams. Low-power density tentacles radiating from the beam were CT artifacts that resulted from the finite number of slits in the 17-slit EMFC diagnostic disk.

Second-Moment Calculation of Beam Diameter

When the beam cannot be described by simple Gaussian or other expressions, a second-moment calculation of the power density distribution can be performed to estimate the beam diameter, generally reported as a D4σ value. This method is described in detail in the ISO 11146-1 laser beam standard, where the beam diameter is defined by a calculation that was originally developed to compare different transverse electromagnetic laser modes in which there isn't necessarily one central peak (Ref. 19). The second-moment calculation can easily be performed if the beam current density is in an x, y array with the power density given at each x and y position, J(x,y). Just like the EMFC, the first moment is initially com-puted to determine the centroid of the distribution defined by the X and Y coordinates (defined by capital X and capital Y) per Equations 3 and 4:
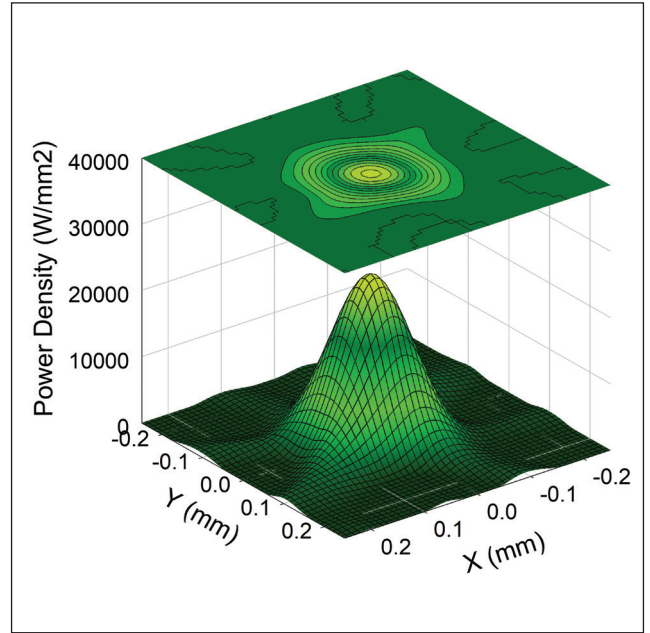

Fig. 5 — An EMFC 3D reconstructed sharp-focused, 120-kV, 5-mA beam from Fig. 3C, with its corresponding contour plot having a PPD of 24,900 W/mm².

$$X = (\Sigma J(x,y)x)/(\Sigma J(x,y)) \qquad (3)$$

$$Y = (\Sigma J(x,y)y)/(\Sigma J(x,y)) \qquad (4)$$

Once the distribution central peak (X,Y) is known, the second moment is calculated for each axis of a simple astig-matic beam, as defined by Equations 5 and 6. These equations define a standard deviation, σ, that characterizes the distri-bution and will be different along the two principal axes for a noncircular, elliptical distribution:

$$\sigma_x^2 = (\Sigma J(x,y)(x - X)^2)/(\Sigma J(x,y)) \qquad (5)$$

$$\sigma_y^2 = (\Sigma J(x,y)(y - Y)^2)/(\Sigma J(x,y)) \qquad (6)$$

The overall standard deviation is then calculated as the square root of the sum of the squares of the standard devi-ations along the x and y axes, as follows:

$$\sigma = \sqrt{\sigma_x^2 + \sigma_y^2} \qquad (7)$$

Table 3 — EMFC Results Compared to Second-Moment Calculations for 1-kW (10-mA, 100-kV) Beams over a ~ 5× Change in Beam Diameter above and below Sharp Focus

|			EMFC				Second Moment
Relative Focus	PPD	FWHM*	FWe2*	FWe2*/ FWHM*	Gaussian Fit	D4σ	D4σ/FWe2*
mA	W/mm²	mm	mm		R^2	mm	—
–50	827	0.97	1.737	1.79	0.990	2.085	1.20
–40	1173	0.836	1.454	1.74	0.993	1.778	1.22
–30	1958	0.652	1.116	1.71	0.990	1.493	1.34
–20	4283	0.395	0.801	2.03	0.995	1.088	1.36
–10	12,594	0.245	0.437	1.78	0.994	0.579	1.32
–5	20,639	0.222	0.360	1.61	0.998	0.432	1.20
0	21,312	0.205	0.337	1.64	0.999	0.412	1.22
5	14,787	0.227	0.399	1.76	0.999	0.524	1.31
10	8791	0.287	0.523	1.82	0.995	0.66	1.26
20	4444	0.413	0.759	1.84	0.999	0.913	1.20
30	1922	0.633	1.143	1.81	0.999	1.346	1.18
40	1133	0.836	1.477	1.77	0.998	1.661	1.12
50	749	0.987	1.83	1.85	0.995	2.095	1.14
Avg./STD	—	—	—	1.78/0.104	0.996/0.003	—	1.24/0.075
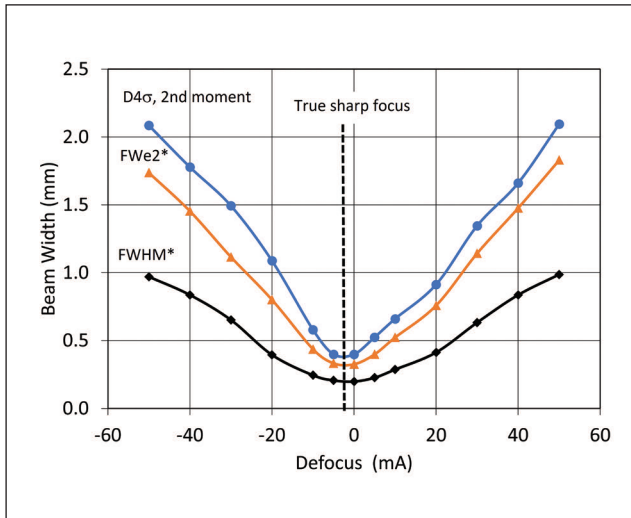
Fig. 6 — Plots of the EMFC-measured beam distributions (FWHM* and FWe2*) compared to the calculated D4σ beam diameter for 13 beams (10 mA, 100 kV).

Fig. 7 — Comparison between the EMFC-measured PPD and the ideal value calculated from FWe2*.

Once σ is known, the overall diameter of the distribution, D, can be calculated from the following equation:

$$D = 2\sqrt{2} * \sigma \qquad (8)$$

For a perfectly circular beam where $\sigma_x = \sigma_y$, D reduces to a value of four times the standard deviation of the beam and is referred to as D4σ, containing 86.5% of the beam's power with 13.5% of the power outside this diameter representing the tails of the distribution

For noncircular distributions, D will be larger than the ideal circular value where D4σ = FWe2 since points that lie outside the ideal circle are weighted more heavily in the second-moment calculation as a result of the squared factors in Equations 5 and 6. This means that the tails of the distribution will be factored in more heavily in the second-moment calculation, but it is not always clear how much of an effect they have on the final weld geometry. It is important to keep in mind which calculation method is being used when comparing beams measured by different methods to take into account the possibility of a given beam having different reported diameters based on the calculation method.

Comparisons between FWe2 and Second-Moment Beam Diameters

To quantify the difference between FWe2 and D4σ, a series of beam diagnostic measurements was made using the EMFC, and then the data was further postprocessed to perform the second-moment calculation of the beam diameter and compare the results. Electron beam welding machine HS#605 was used again with the same ribbon filament setup that was used to generate the images in Figs. 1 and 3 but with a lower voltage 1.0-kW (100-kV, 10-mA) beam and at a longer work
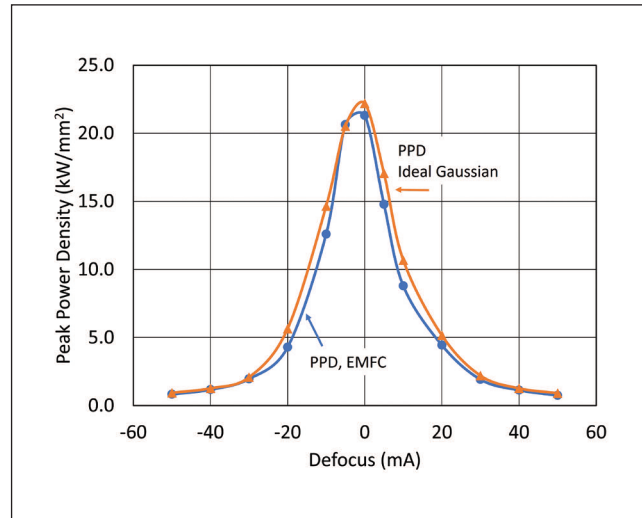
distance of 8 in. (203 mm), which corresponds to a focal length of 267 mm (10.51 in.) on this machine. For a point of reference, the work distance is the distance from the top of the electron beam chamber to the EMFC diagnostic slit disk, and for this welding machine, the top of the chamber sat 2.5 in. (64 mm) below the final focusing lens (Ref. 11).

The data were taken by defocusing the beam from –50 to +50 mA relative to the sharp-focused (681 mA) condition. Thirteen beams were analyzed, showing a ~ 5× increase in beam diameter from its sharp-focused minimum size, as summarized in Table 3. These data are further plotted in Fig. 6, which compares FWHM*, FWe2*, and D4σ. Note that the true sharp focus for this beam is located approximately at –2 mA based on where the minimum in the curves might be expected as the beam passes through a waist. The results show that FWHM* varied from 0.21 mm (0.008 in.) at the sharp focus to approximately 1 mm (0.039 in.) at the +50 and –50 defocus settings and was reasonably symmetric about the true sharp-focus position for overfocus and underfocus settings. The FWe2* varied from 0.34 mm (0.013 in.) at sharp focus to 1.8 mm (0.071 in.) at the +50 and –50 defocus settings and was also reasonably symmetric about the true sharp-focus position.

For an ideal Gaussian beam, the ratio of FWe2 to FWHM would be equal to 1.70 (4σ/2.35σ). The average value for the 13 beams studied here was calculated to be 1.78 ± 0.104, which is close to the ideal value. This ratio confirmed that the electron beams were reasonably Gaussian-shaped and that either FWe2* or FWHM* could be used as a predictor of the power density distribution. However, the FWe2* beam diameter was recommended for comparison to lasers and other diagnostic methods that use beam diameter instead of FWHM* for characterization. The individual profiles were further fit to an ideal Gaussian shape, as was done in Fig. 4, where the results are summarized in Table 3, showing R^2 values varying from 0.996 ± 0.003 as well as indicating a good fit and a strong Gaussian distribution to the beams.

Table 4 — Measured Beam Properties as a Function of Distance along Propagation Axis of a 1-kW (10-mA, 100-kV) Beam for a 267-mm-Focal-Length Beam at Crossover with Lens Current of 684 mA

| Z-Axis Relative to Beam Crossover	FWHM*	FWe2*	D4σ	PPD
mm	mm	mm	mm	W/mm²
–5.1	0.22	0.37	0.467	19,080
–2.5	0.22	0.36	0.455	19,186
0.0	0.21	0.36	0.449	20,140
2.5	0.21	0.36	0.448	19,716
5.1	0.22	0.36	0.450	19,080
7.6	0.23	0.39	0.477	17,172
10.2	0.25	0.43	0.526	13,462
12.7	0.27	0.46	0.561	11,978
15.2	0.28	0.48	0.603	9752
17.8	0.31	0.52	0.64	7473
20.3	0.33	0.58	0.734	6848
22.9	0.36	0.63	0.781	6307
25.4	0.38	0.68	0.851	5639
27.9	0.41	0.73	0.925	4844
30.5	0.46	0.83	1.038	3805
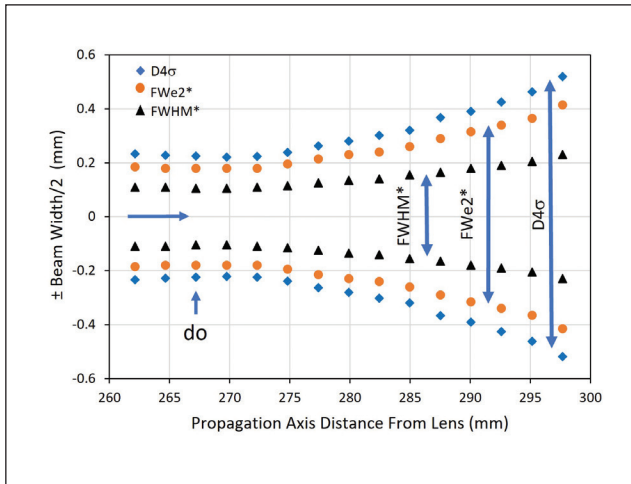
Fig. 8 — Electron beam caustic based on FWHM*, FWe2*, and D4σ, showing their respective divergence below the beam crossover for a 1-kW electron beam at a focal length of 267 mm.
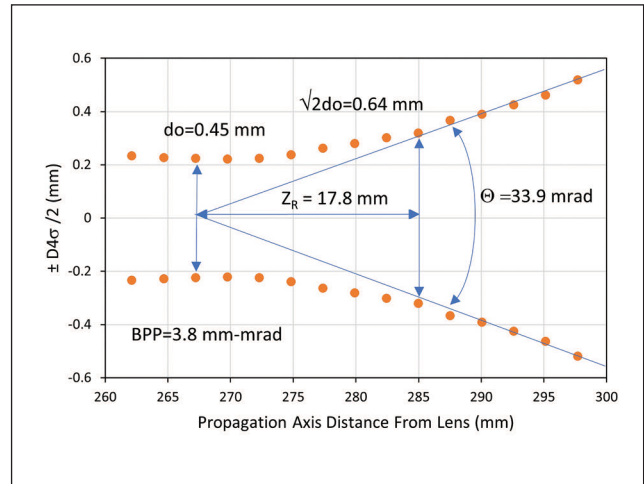

Fig. 9 — Electron beam caustic showing beam divergence below the beam crossover for a 10-mA, 100-kV electron beam at a focal length of 267 mm. The BPP calculates to be 3.8 mm-mrad for this beam based on D4σ.

Table 5 — Summary of Beam Caustic Measurements Based on Different Measurements of the Beam Widths

Measurement Basis	do	Full Angle Θ	BPP	Z_R
	mm	mrad	mm-mrad	mm
FWHM*	0.22	14.9	0.82	17.8
FWe2*	0.36	27.1	2.44	17.3
D4σ	0.45	33.9	3.81	17.8

Note: D4σ would correspond to ISO 11146 for second-moment calculation used for laser beams.

From the graphed data in Fig. 6, D4σ is calculating larger beam diameters than FWe2*, which was expected due to the Gaussian tails being weighted more in the second-moment calculation method. Table 3 further compares the ratio of the two measurements, showing that D4σ is 1.24 ± 0.075 larger than FWe2* over this range of defocus settings. For this beam, D4σ laid closer to FWe2* for overfocus settings than for underfocus settings. This was the result of the skewing of the underfocused beam, as discussed previously and highlighted in Fig. 3, and is further indication that beam propagation does not always follow a symmetric caustic around the minimum beam diameter in the electron beam chamber.

A similar comparison between the EMFC FWe2* and the calculated D4σ was made in a different study by Pierce and Burgardt at Los Alamos National Laboratory (Ref. 20). In their study, a 60-kV-maximum (low-voltage) Probeam electron beam welding machine was used with a different gun and cathode arrangement than the LLNL welding machine and was operating at 60 kV instead of 100 kV. The results showed that the beams were also largely Gaussian-shaped and that D4σ was consistently about 1.35 times larger than the FWe2* on their low-voltage machine (Ref. 20). The larger difference between FWE2* and D4σ (1.35 vs. 1.24) on the low-voltage machine was likely due to a halo of low-density electrons

surrounding the core of the electron beam that formed in this gun and cathode design and contributed more to D4σ than on the LLNL high-voltage machine (Ref. 20). However, their findings overall confirmed the results of this study in that D4σ was consistently larger than FWe2* for a given machine but also pointed out that different electron beam welding machines had subtle differences in the power density distributions of beams that were generated. The conclusions made by Pierce and Burgardt also indicated that the core of the electron beam was what influenced the weld characteristics the most, and the low-density electron halo or Gaussian tails may not have had a large effect on the overall weld keyholing and penetration characteristics.

Another comparison that can be made is the relationship between the measured PPD and what would be predicted for an ideal Gaussian beam using the measured beam diameter. Based on the beam's profile, the EMFC-measured PPD should be closely correlated to a Gaussian shape. To calculate the PPD of an ideal circular Gaussian beam from its diameter, the current density distribution relationship of Equation 1 was integrated over the x-y plane and used to equate the Gaussian standard deviation σ to FWe2, yielding the following relationship between the PPD and FWe2*:

$$PPD = (8\, I_0\, V)/\pi (FWe2^*)^2 \qquad (9)$$

In this equation, I_o is the peak current density of the beam and V is the accelerating voltage of the beam. Figure 7 shows this comparison for the 13 beams, where the PPD measured by the EMFC was plotted against its ideal peak based on the FWe2* diameter. The results indicated that the ideal PPD and the measured PPD are very closely related, with the ideal value being slightly larger by 4% on average (PPD ideal/PPD measured = 1.040 ± 0.051). An interesting observation can be made on the shape of the PPD vs. defocus setting. Although the PPD curve appears to have a Gaussian shape with defocus, in principle it will follow Equation 9, being inversely proportional to the square of the beam diameter. Because of this relationship, PPD was highly sensitive to changes in the beam diameter and was a good indicator to find the sharpest-focused beam that was used as a reference point for process control.

Beam Divergence at a Fixed Focal Length

The propagating electron beam converges and diverges from the sharp-focus point, as illustrated in Fig. 2. The full beam angle Θ, at which the beam approaches the focal spot, was related to the beam diameter at the final focusing spot and the focal length to the sharp-focus position in the same way that laser beams are defined after passing through the final focusing lens (Ref. 8). When changing the electron beam spot size by adjusting the focus coil current, the beam properties varied, as illustrated in Fig. 6. However, Θ was not fixed by the method, shown in Fig. 6, because the focal distance of the beam and its minimum diameter were both changing as the sharp-focal position moved up or down relative to the initial sharp-focus condition. Because of this, the beam caustic could not be precisely determined by analyzing the beam at one work distance only and required analysis of the beam at different distances away from its fixed sharp-focused crossover location.

To demonstrate this, a final set of measurements was made to determine the beam divergence angle and corresponding beam parameter product by analyzing a series of beams at different distances above and below a fixed focal length beam using a z-axis stage to move the EMFC diagnostic relative to the crossover spot in the chamber. In this set of experiments, the beam was again set at a 267-mm focal length for the 1-kW (100-kV, 10-mA) beam. Electron optics suggest that the beam converges and diverges to its sharpest focal position linearly with the propagation axis at a full beam angle, Θ, which can be defined for an ideal circular stigmatic beam as follows (Ref. 8):

$$\Theta = \lim_{(z-zo)\to\infty} \left(\frac{do\,(z)}{(z-zo)} \right) \qquad (10)$$

In Equation 10, do(z) is the beam diameter at a distance (z-zo) from the sharp-focus z-axis location zo. Note that for small angles, such as laser or EB, that incorporate long focal length lenses, this approximation can be made for the more-accurate trigonometric function. For simple astigmatic beams, Equation 10 can be replaced with separate equations along the principal x and y axes of the ellipse and modified for their separate diameters and focal lengths (Ref. 8). Table 4 summarizes the beam analysis measurements that were made on the 1-kW beam as a function of distance from the beam crossover location. These data are further plotted in Fig. 8, illustrating and quantifying the minimum spot size, do, and beam divergence angle based on FWHM*, FWe2*, and D4σ downstream of the crossover location. The difference between the measurements was clear, showing that the largest beam diameter and largest divergence angle were for the D4σ measurement.

The divergence of the beam and its smallest spot size can be combined and used as a measure of beam quality identical to that of laser beams (Ref. 8). This factor is the beam parameter product (BPP), which is defined as the half-angle divergence times the minimum beam radius and is calculated from the full divergence angle and minimum beam diameter as follows (Ref. 2):

$$BPP = do * \Theta * 0.25 \qquad (11)$$

To compare the electron beam diameters to lasers using the ISO 11146-1 standard, D4σ was used to represent the do in this equation. Figure 9 shows the beam divergence plot for this data set, where the divergence angle was determined using a linear fit to the data from the far-field to the crossover point of the beam. The results showed that Θ = 33.9 mrad (full angle per Equation 10) and BPP = 3.8 mm-mrad per Equation 11 for the minimum D4σ spot size of do = 0.45 mm (0.017 in.). Furthermore, the Rayleigh length (Z_R), which corresponds to a doubling of the beam area from the smallest beam diameter (do) at crossover to a beam diameter equal to √2do, was calculated to be Z_R = 17.8 mm (0.701 in.). This

beam quality was on the high-intensity end (lower BPP) of multimode high-power-fiber laser beams, where BPP ranged from approximately 2–10 mm-mrad, depending on the optical configuration (Ref. 21). Similar beam qualities should result in similar electron beam vs. laser weld penetrations for given spot sizes for laser welds performed under reduced pressure conditions (i.e., laser in vacuum), as shown in a previous study (Ref. 21).

One final comparison was made and is summarized in Table 5, which shows the D4σ beam properties relative to those calculated from FWHM* and FWe2*. Since FWe2* was approximately 1.7× larger than FWHM*, the FWe2* minimum beam diameter and its divergence angle were approximately 1.7× larger than FWHM*. Correspondingly, D4σ was approximately 1.24× larger than FWe2*, so its minimum beam diameter and divergence angle were both approximately 1.24× larger than FWe2*. This results in a wide range of BPP as determined from each of the widths measurements, between 0.82 and 3.8 mm-mrad, which points out the significance of comparing similar beam diagnostic measurements when reporting BPP for different beams or setup configurations.

Summary and Conclusions

Electron beams generated by the LLNL electron beam welding machine HS#605 at 100 and 120 kV were analyzed using the EMFC diagnostic to show relationships between defocus settings, beam dimensions, and peak power densities (PPDs). These data were compared to the ISO 11146-1 standard, second-moment calculation method, for laser beam propagation, and the following conclusions were made:

1) Analysis showed that the beams are largely Gaussian-shaped, having a central peak and a power density distribution that can be described using conventional Gaussian mathematics with high confidence of fit for the profiles. The FWHM, FWe2, and PPD properties can all be related to the beam's power and standard deviation of a Gaussian distribution.

2) Astigmatism of the beam was shown to be present, skewing the beam from more of a circular Gaussian shape into an elliptical Gaussian shape that can be measured and quantified. The elliptical beam shape rotated 90 deg as the beam passed through its crossover point at sharp focus and was more circular near sharp focus than in the defocused conditions.

3) The beam diameter measured by the EMFC diagnostic, FWe2*, represents 86.5% of the beam's power and was identical to the D4σ beam diameter for an ideal circular Gaussian laser beam as defined by the second-moment calculation of the ISO 11146-1 standard. For noncircular or nonideal Gaussian shapes, D4σ was calculated to a larger diameter than FWe2* due to the higher weighing of the tails of the distribution by the second-moment calculation method. In the experiments performed here at 100 kV, D4σ calculated to be approximately 25% larger than FWe2*.

4) Defocusing experiments at ± 5× the sharpest focused beam diameter were performed on a 1-kW (100-kV, 10-mA) beam to map changes in FWHM*, FWe2*, and D4σ with a focus setting that varied the focal length. The results showed

nearly mirror-image defocus results on the sharpest focus condition that had a minimum beam diameter of FWe2* = 0.37 mm (0.014 in.) but with some asymmetry where under-focus settings relative to sharp showed a larger separation between FWe2* and D4σ due to nonsymmetric skewing of the electron beam power distribution.

5) The power density distribution was further measured as a function of focus setting for the 1-kW (100-kV, 10-mA) beam and was shown to be close to the ideal value based on a perfect Gaussian shape. The beam's power density peaked at about 21,000 W/mm^2 at sharp focus and dropped below 1000 W/mm^2 for the highest defocused beam. The ~ 20× change in PPD was more sensitive to focus setting than the beam diameter, allowing it to be used as an additional, and perhaps more accurate, predictor of the sharpest focused beam condition.

6) The beam properties were further examined at a fixed focus length of 267 mm to determine the caustic for the 1-kW (100-kV, 10-mA) beam by measuring the beam at different distances away from its sharp crossover position. The results gave the full divergence angle of Θ = 33.9 deg, minimum diameter do = 0.45 mm, BPP = 3.8 mm-mrad, and Rayleigh length R_z = 17.8 mm, based on the D4σ measured beam properties. This BPP was similar to multimode fiber optic-delivered laser beams produced using small diameter fibers at similar focal lengths.

Competing Interests

The authors declare that they have no known competing financial interests or personal relationships that could have appeared to influence the work reported in this paper.

References

1. American Welding Society. 2008. *Welding Handbook*, Ninth Edition, Volume 3, Welding Processes, Part 2. Miami, Fla.

2. Schultz, H. 2018. *Electron Beam Welding: Principles, Equipment and Operation*. English Edition, Vol. 14. Dusseldorf, Germany: DVS Media GmbH.

3. Elmer, J. W., Teruya, A. T., and O'Brien, D. W. 1993. Tomographic imaging of noncircular and irregular electron beam power density distributions. *Welding Journal* 72(11): 493-s to 505-s.

4. Elmer, J. W., and Teruya, A. T. 2001. An enhanced Faraday cup for the rapid determination of the power density distribution in electron beams. *Welding Journal* 80(12): 288-s to 295-s.

5. Dutilleul, T., Priest, J., and Baufeld, B. 2016. Electron beam characterisation. *Elektronika ir Elektrotechnika (E+E)* 51(5–6): 175–183.

6. Elmer, J. W., Giedt, W. H., and Eagar, T. W. 1990. The transition from shallow to deep penetration during electron-beam welding. *Welding Journal* 69(5): 167-s to 176-s.

7. Rai, R., Palmer, T. A., Elmer, J. W., and Debroy, T. 2009. Heat transfer and fluid flow during electron beam welding of 304L stainless steel alloy. *Welding Journal* 88(3): 54-s to 61-s.

8. ISO 11146-1:2021 (En), Lasers and laser-related equipment — Test methods for laser beam widths, divergence angles and beam propagation ratios — Part 1: Stigmatic and simple astigmatic beams.

9. Elmer, J. W., Hochanadel, P. W., Lachenberg, K., Caristan, C., and Webber, T. 2011. *ASM Handbook of Welding*, Vol. 11. pp. 522–539.

10. American Welding Society. 2004. AWS C7.1M/C7.1:2004, *Recommended Practices for Electron Beam Welding*. Miami, Fla.

11. Palmer, T. A., and Elmer, J. W. 2007. Characterization of electron beams at different focus settings and work distances in multiple welders using the enhanced modified Faraday cup. *Science and Technology of Welding and Joining* 12(2): 161–174. DOI: 10.1179/174329307X176631

12. Palmer, T. A., Elmer, J. W., Nicklas, K. D., and Mustaleski, T. 2007. Transferring electron beam parameters using the enhanced modified Faraday cup. *Welding Journal* 86(12): 388-s to 398-s.

13. Elmer, J. W., Terrill, P., and Butler, D. 2002. Joining depleted uranium to high-strength aluminum using an explosively clad niobium interlayer. *Welding Journal* 81(8): 167-s to 173-s.

14. Teruya, A., Elmer, J. W., and O'Brien, D. 1991. A system for the tomographic determination of the power distribution in electron beams. U.S. Patent US5382895, filed 1 August 1994 and issued 21 November 1995. *osti.gov/doepatents/biblio/6614602*

15. Elmer, J. W., and Teruya, A. T. 1998. Fast method for measuring power density distribution of non-circular and irregular electron beams. *Science and Technology of Welding and Joining* 3(2): 51–58. DOI: 10.1179/stw.1998.3.2.51

16. Elmer, J. W., and Gibbs, G. 2003. Astigmatic electron beam propagation. *Science and Technology of Welding and Joining*. DOI: 10.1080/13621718.2023.2198787

17. Kenichi, I. 1994. *Fundamentals of Laser Optics*. New York, N.Y.: Springer.

18. Palmer, T. A., and Elmer, J. W. 2008. Improving process control in electron beam welding using the enhanced modified Faraday cup. *Journal of Manufacturing Science and Engineering, Transactions of the ASME* 130(4): 410081–4100815. DOI: 10.1115/1.2950061

19. Paschotta, R. 2008. *Encyclopedia of Laser Physics and Technology*, 640-643. Weinheim, Germany: Wiley-VCH.

20. Pierce, S. W., and Burgardt, P. 2014. Evaluation of two devices for electron beam profiling. Los Alamos National Laboratory, Los Alamos, N.Mex. DOI: 10.2172/1163630

21. Elmer, J. W., Vaja, J., and Gibbs, G. 2022. Reduced-pressure laser weld comparison to electron beam welds in Ti-6Al-4V. *Welding in The World* 66: 2053–2071. DOI: 10.1007/s40194-022-01356-8

JOHN W. ELMER (*elmer1@llnl.gov*), **ALAN T. TERUYA,** and **GORDON GIBBS** are with the Lawrence Livermore National Laboratory, Livermore, Calif.

Can We Talk?

The *Welding Journal* staff encourages an exchange of ideas with you, our readers. If you'd like to ask a question, share an idea, or voice an opinion, you can call, write, or email. Staff email addresses are listed below, along with a guide to help you interact with the right person.

Publisher/Editor
Annette Alonso, *aalonso@aws.org*, (786) 937-9599
General Management, Reprint Permission,
Copyright Issues, Editorial Content

Managing Editor
Kristin Campbell, *kcampbell@aws.org*, (786) 937-9557
Feature Articles

Sr. Editor
Cindy Weihl, *cweihl@aws.org*, (786) 937-9556
Section News, *SPRAYTIME*®

Associate Editors
Alexandra Quiñones, *aquinones@aws.org*, (786) 937-9623
Arc-Tist Corner, Industry News
Katie Pacheco, *kpacheco@aws.org*, (786) 937-9575
Society News, New Products

Education Editor
Roline Pascal, *rpascal@aws.org*, (786) 937-9603
Coming Events, Personnel

Managing Editor, Digital and Design; Editor of *Inspection Trends and Welding Journal en Español*
Carlos Guzman, *cguzman@aws.org*, (786) 937-9503
Inspection and Spanish-Language Content,
Design and Production

Production Manager
Zaida Chavez, *zaida@aws.org*, (786) 937-9565
Design and Production

Assistant Production Manager
Brenda Flores, *bflores@aws.org*, (786) 937-9630
Design and Production, Peer Review Coordinator

Advertising
Scott Beller, *sbeller@aws.org*, (786) 937-9619
Lea Owen, *lea@aws.org*, (786) 937-9520

Subscriptions
Giovanni Valdes, *gvaldes@aws.org*, (786) 937-9629